Earth Science Informatics (2025) 18:322
https://doi.org/10.1007/s12145-025-01829-6

SOFTWARE

Design and evaluation of a cloud-oriented procedure based on SAR and Multispectral data to detect burnt areas

Cristina Vittucci[1] · Flavio Cordari[2] · Leila Guerriero[1] · Pierangelo Di Sanzo[3]

Received: 7 September 2024 / Accepted: 27 February 2025 / Published online: 11 March 2025

Abstract

This article presents the design and an experimental evaluation study of a novel procedure based on the synergistic use of SAR and Multispectral data to detect burnt area over vegetated natural surfaces. The procedure is designed to take advantages of open satellite datasets and cloud computing services. The underpinning data processing workflow exploits the variation of the backscattering coefficients and the spectral signature of surfaces affected by fire damages by applying a threshold-based technique optimized for different land cover classes. The presented experimental study focuses on three large wildfires occurred over Europe during the last four years. By comparing the burnt areas detected by the procedure with data from the European Forest Fire Information Service, we obtained an overall accuracy higher than 0.88 for all the considered test cases. The presented data also include various metrics that allow to compare the results achievable by using in synergy SAR and Multispectral data with respect to the individual use of them. Overall, the results of our study show that the presented procedure, and more in general the exploited design approach, can be of interest for researchers and practitioners for the development of efficient automated solutions for the detection of burnt areas.

Keywords Burnt area detection · Multispectral imaging · SAR imaging · Cloud computing · Copernicus sentinel data

Introduction

Every year, a large amount of natural vegetated areas are burned by wildfires. As an example, over the last decade the total area burned in Europe ranged from 300,000 to 1,000,000 hectares per year. Various techniques exploiting satellite remote sensing were proposed to monitor changes triggered by natural calamities, including wildfires. However, remote sensing of burnt areas faces several challenges hindering accurate mapping across diverse landscapes. These include limitations in spatial resolution, where coarse imagery misses small burns and moderate resolution is impacted by phenology and cloud cover (Liu et al. 2023). Atmospheric interference from clouds and shadows further complicates detection (Laneve et al. 2023). Variability in post-fire spectral responses across different land cover types (forests, grasslands, etc.) also poses a significant challenge (Liu et al. 2023; Arnaudo et al. 2023). Maintaining data consistency and continuity for long-term monitoring is additionally difficult due to variations in satellite data quality and availability (Chen et al. 2024). Solutions to these challenges include advanced algorithms integrating multiple temporal scales and spectral indices, such as combining single-, dual-, and short-time series images (Liu et al. 2023). Multisource data integration from satellites like MODIS, VIIRS and Sentinel-2, can offer a more comprehensive dataset for burnt area detection (Liu et al. 2023). Further, multitask learning frameworks incor-

Communicated by: Hassan Babaie

✉ Cristina Vittucci
cristina.vittucci@uniroma2.it

✉ Pierangelo Di Sanzo
pierangelo.disanzo@uniroma3.it

Flavio Cordari
flavio.cordari@uniroma1.it

Leila Guerriero
leila.guerriero@uniroma2.it

[1] Department of Civil Engineering and Computer Science Engineering, Tor Vergata University of Rome, Via Politecnico, 1, Roma 00133, Italy

[2] Department of Civil, Building and Environmental Engineering, Sapienza University of Rome, Via Eudossiana, 18, Roma 00184, Italy

[3] Department of Economics, Roma Tre University, Via Silvio D'Amico, 77, Rome 00145, Italy

porating auxiliary tasks like land cover classification can enhance model robustness (Arnaudo et al. 2023), and ground validation using survey data refines satellite-based estimates (Laneve et al. 2023).

Recent advancements improved accuracy and efficiency in burnt area detection through the integration of deep learning and high-resolution imagery. Deep learning models, such as Convolutional Neural sinergy Networks (CNNs), demonstrated superior performance compared to traditional methods like the Normalized Burn Ratio (NBR) when adequate training information are accessible (Anand et al. 2024). The availability of high-resolution satellite images, such as PlanetScope and Sentinel-2, may allow for more detailed analysis (Kim et al. 2024). Transfer learning can further enhance model performance by leveraging knowledge across datasets, improving detection capabilities across different regions (Seo and Lee 2024).

Other techniques are based on high resolution Multispectral (MS) optical imagery, as provided by Landsat 8 and 9 or Sentinel-2 missions, exploiting variations in brightness between the near-infrared (NIR) and short-wave infrared (SWIR) bands to track changes in forest cover (Lima et al. 2019). In this context, some techniques were proposed to map the effects of wildfires with Sentinel-2 data by exploiting the variation of spectral indices computed before and after an event (Giorgos Mallinis and Chrysafi 2018; Phiri et al. 2020; Huang et al. 2016). Among the techniques based on spectral indices, the Normalized Difference Vegetation Index (NDVI), which utilizes the Sentinel-2 R and NIR bands, and the differenced Normalized Burnt Ratio (dNBR), based on NIR and SWIR bands, are the most widely adopted ones for mapping the areas affected by fires and the severity of their effects (Smiraglia et al. 2020; Fernández-Manso et al. 2016). While MS optical sensors are effective in many cases, they are limited by cloud cover and illumination conditions. Synthetic Aperture Radar (SAR) products offer an alternative solution, as they are unaffected by clouds or light conditions, maintaining a sensitivity to the presence of trees, at L, C and X bands (Santi et al. 2017). However, SAR sensors also have drawbacks, like speckle and geometric distortion. Despite these limitations, many successful applications of SAR data for forest monitoring were developed with different radar missions (Tanase et al. 2010; Kurbanov et al. 2022).

Copernicus (EU 2024) Sentinel-1, a C-band SAR mission, revolutionized forest monitoring by providing rapid revisit times and spatial resolution of 10 meters, demonstrating the important role of such data to monitor wildfires using both backscattering and phase signal-based analysis (Imperatore et al. 2017; Belenguer-Plomer et al. 2019; Lasaponara and Tucci 2019; Donezar et al. 2019). More recently, the use of various data products, like Sentinel-1, Sentinel-2 and Landsat 8 data, were evaluated in some research studies exploiting ML-based and numerical algorithms (Brown et al. 2018; Tanase et al. 2020; Gibson et al. 2023; Zhang et al. 2021; Arjasakusuma et al. 2022), showing that the combination of both SAR and MS data may provide additional advantages. SAR information can compensate the limitation due to cloud cover and variation of surface solar radiation of MS measurements, while the latter are useful where SAR lose sensitivity due to topography effects, or over areas with low volumetric backscattering. However, the results obtained by the various studies do not agree on the effectiveness of the combined use of these data products. Moreover, from an operational point of view, the proposed ML-based solutions have the disadvantage of requiring large and accurate training data sets to provide sufficiently accurate results.

This article presents the design and an evaluation study of a novel procedure to detect burnt areas over vegetated natural surfaces based on a synergistic usage of multiple open data products, in particular combining SAR and MS data. It uses Sentinel-1 and Sentinel-2 images, and is supported by Corine Land Cover (CLC) data, leveraging specific thresholds for different land cover classes to maximize the accuracy. Additionally, the procedure is designed to efficiently exploit cloud computing services, relying on control scripts that automate the access to the computing resources offered by the cloud infrastructure and the software environment configuration. This allows to take advantage of the several public cloud platforms that offer pay-per-use computing resources and provide free and fast access to Copernicus data, like Amazon Web Services (AWS, Amazon 2024), Google Cloud (Google 2024), as well as the various Copernicus Data and Information Access Services (DIAS 2024) in Europe.

The experimental evaluation study we present in this article evaluates the advantages, in terms of prediction accuracy and other specific metrics, achievable with the proposed procedure through the combined use of SAR and MS data. The study is focused on three large wildfires occurred over Europe during the last four years. We compared the burnt areas detected by the procedure with the official burnt area maps of the European Forest Fire Information System (EFFIS). The latter is the primary source of information about European wildfires developed by the Joint Research Centre (JRC) and the Copernicus Emergency Mapping Service (EMS) (Giglio et al. 2003; Roy et al. 2005, 2007; Navarro et al. 2017). The results show that the procedure achieved a detection accuracy greater than 0.88 over all the considered test cases. Furthermore, they show that better results can be achieved using SAR and MS data in combination rather than individually.

In summary, the contribution of this article includes:

- The design of a new burnt area detection procedure that uses different types of open data products in a synergistic way. Moreover, being designed to offer high simplicity in

the deployment and operation on public cloud platforms, it can be easily used by anyone for experimentation and research purposes.

- An experimental study of the proposed procedure, performed on recent wildfire events, which provides a number of evaluation metrics. In particular, the calculated metrics allow to compare the results achievable from the combined use of SAR and MS data versus the individual use of these data.
- An open source software implementation of the procedure workflow, thus freely available to anyone for evaluation and reuse.

In the following of this article, we first provide the details about the data products used by the procedure, then we present the procedure design and the implementation details. Finally, we report the results of the experimental evaluation study and a final discussion on the overall results of the presented study.

Data products

The procedure is designed to exploit open data from one of the various available Copernicus data repositories. First,

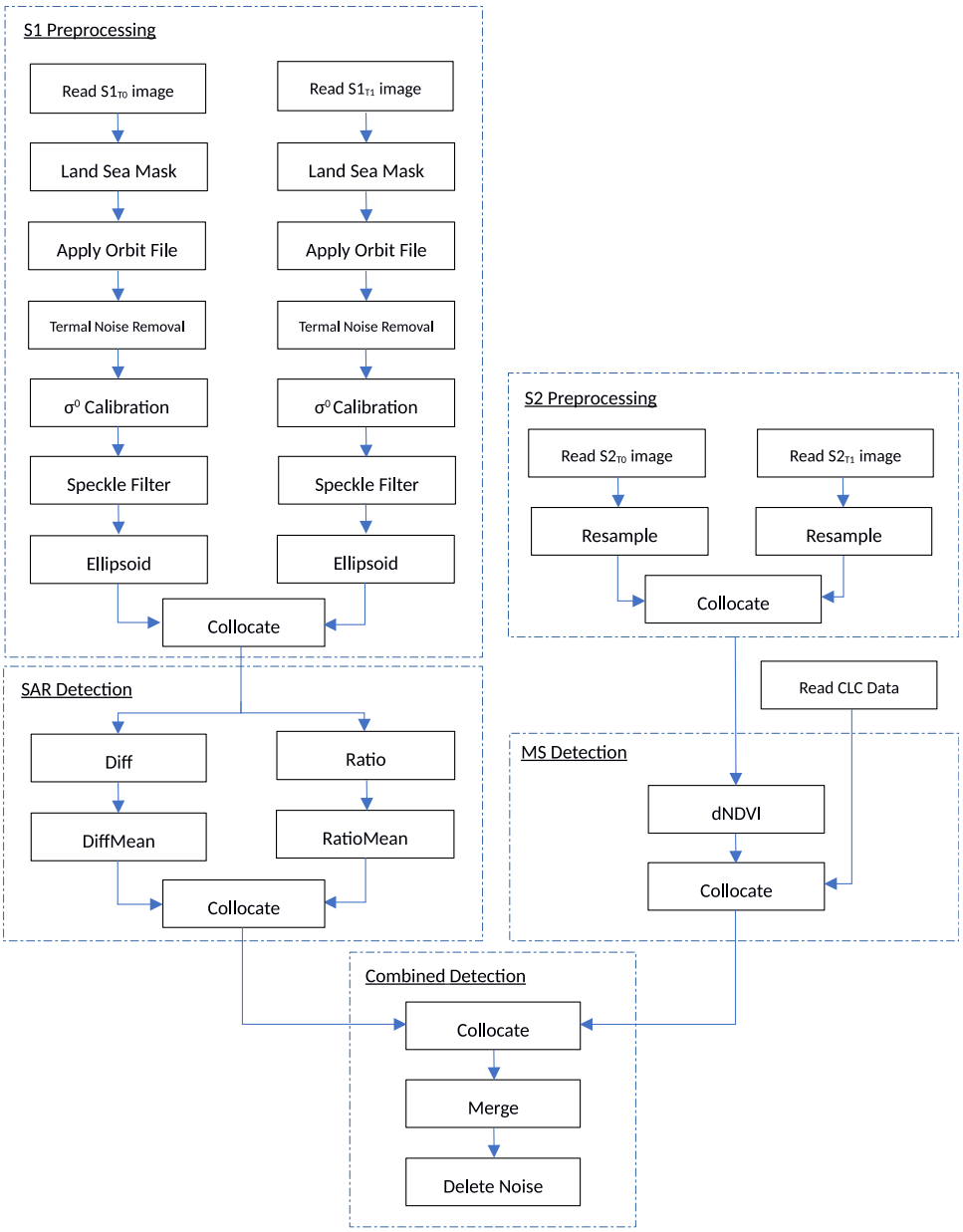

Fig. 1 The data processing workflow underpinning the proposed procedure. Sentinel-1 and Sentinel-2 are denoted as S1 and S2, respectively

it uses Sentinel-1 L1 Ground Range Detected (GRD) data, which have a nominal spatial resolution of 10m and provide both amplitude and phase information. These products are presented in slant-range geometry, with a preprocessing operation applied before deriving radar features to reproject measurements on a reference ellipsoid representing the planet geoid. Further, the procedure uses Sentinel-2 Level-2A (L2A) data (processed from L1C with Sen2Cor), which offer orthorectified Surface Reflectance data at the Bottom of Atmosphere (SR BOA), providing valuable insights into Earth's inherent properties, independent of atmospheric effects. L2A products also include a scene classification band (i.e. categorization of different land cover types, including clouds, water, and vegetation), which is exploited for fast application of masking areas in the data processing workflow. Finally, it uses data from CLC, a standardized inventory of land cover information in Europe, which provides insights for environmental and land-use studies. The spatial resolution is 100m, with a minimum mapping unit of 25 hectares, making it suitable for precise land cover information. Despite land cover products with higher spatial resolution than CLC are available, we decided to use CLC as a trade-off among spatial resolution, data size and open accessibility. For the experimental evaluation study, we used data from EFFIS, which offer reliable and state-of-the-art information about burnt area detection, perimeter mapping and burnt severity assessment for all the major wildfire events in Europe. It is considered as a benchmark for evaluating solutions for fire effects detection using satellite data. We used the more reliable information provided by EFFIS for each of the considered test case, exploiting for the evaluation of the results the consolidated burn grading maps, which provide an assessment of the damage grade and its spatial distribution.

Design and implementation

In the first part of this section, we focus on the design of the proposed procedure. We introduce the underpinning data processing workflow and we discuss the related design choices. Then, we enter into the implementation details of the workflow and of the automatism which allows the procedure to easily exploit computing resources offered by a cloud computing platform.

Procedure design

The procedure is based on the identification of specific differences between two pairs of SAR and MS images, all related to the geographic area under surveillance. Given the peculiarities of Sentinel-1 SAR images, the procedure exploits the percentage variation of the backscattering coefficient, at the two instrument polarizations combinations. Concerning Sentinel-2 data, it leverages the variation of NDVI, computed by using the Red and the NIR bands of Sentinel-2 MSI Instrument. CLC data, which contain the classification of the European territory with respect to different classes of urbanized and natural surface, are taken as input in a subsequent phase of the data processing workflow. With respect to the CLC classes, only those related to forest cover, agriculture crops and low vegetation are considered.

The first Sentinel-1 image of the first pair is denoted as $S1_{T0}$, while its second Sentinel-1 image is denoted as $S1_{T1}$. The first Sentinel-2 image of the second pair is denoted as $S2_{T0}$, while its second Sentinel-2 image is denoted as $S2_{T1}$. The first image of each pair must have been acquired before the time period under surveillance, and the second image of each pair must have been acquired after the time period under surveillance.

The procedure exploits the data processing workflow shown in Fig. 1. Rectangles represent operators that receive input data and produce output data. Arrows represent data flows between operators. Specifically, an arrow from an operator A to an operator B indicates that the operator B receives as input data the output data produced by the operator A. Operators are grouped within phases. Each phase is designed to perform specific data processing objectives. All phases of the workflow are described in detail in the following. In Table 1, we report a specific description of each operator, with the expected input data and the output data.

The first phases evidenced on top of the workflow in Fig. 1 show that input images pass through preprocessing phases, composed of operators offered by the ESA SNAP GPT (ESA 2024a). Sentinel-1 images are preprocessed within the *S1 Preprocessing* phase, using in sequence operators Land Sea Mask (to mask the pixels over sea), Apply Orbit File, Thermal Noise Removal, σ^0 Calibration (to derive the backscattering coefficient from the SAR Amplitude signal), Speckle filtering using GAMMA map 3x3 function kernel (Lopes et al. 1990), and Ellipsoid Terrain Correction. The results are maps of backscattering coefficients (σ^0) at about 100m spatial resolution, reprojected on the WGS84 ellipsoid, at the VH and VV polarizations. After the *S1 Preprocessing* phase, the maps of coefficients σ^0_{VH} and σ^0_{VV} related to $S1_{T0}$ and $S1_{T1}$ are coregistered (by the Collocate operator) then the *SAR Detection* phase (which we describe in detail later in this section) starts.

The *S2 Preprocessing* phase, applied to the two Sentinel-2 images, consists of a resampling operator, that can be applied to resample all MS bands over the 10m spatial resolution grid (useful to implement additional vegetation indices in future developments). Within the resampling operation, a filtering operator based on the Scene Classification (SC)

Table 1 Details about all the operators used in the data processing workflow underpinning the procedure

Operator	Description	Expected Input	Output
Read image/data	Read data from file	A file path	Image data
Land Sea Mask	Masks sea regions	A Sentinel-1 GRD data with sea regions	Masked data with no sea regions
Apply Orbit File	Updates orbit metadata with precise values	SAR metadata with general orbit information	Accurate satellite position and velocity metadata
Thermal Noise Removal	Reduces thermal noise in SAR imagery	Sentinel-1 GRD data with noise artifacts	Data with reduced thermal noise
σ^0 Calibration	Converts pixel values to radiometric backscatter	Uncalibrated Sentinel-1 GRD data	Calibrated backscatter data (sigma nought values)
Speckle Filter	Reduces granular noise (speckle) in images	SAR imagery with speckle noise	Noise-reduced SAR imagery
Ellipsoid	Corrects geometric distortions caused by the Earth's curvature	SAR imagery with distortions	Geometrically corrected imagery referenced to a standard ellipsoid
Collocate	Spatially collocates two or more data products.	Two or more data product spatial.	Spatially collocated data product, where corresponding data points represent the same location.
Resample	Modifies the spatial resolution.	A image with a given spatial resolution.	The image with the new spatial resolution.
Diff	Calculates the pixel-by-pixel difference between two images.	Two images with the same spatial extent.	Data representing pixel-by-pixel differences.
DiffMean RatioMean	Applies a moving filter which calculates the average of all pixels within a 3x3 region.	A noisy image	A filtered (blurred, less noisy) image
Ratio	Calculates the pixel-by-pixel ratio between two images.	Two images with the same spatial extent.	Data representing pixel-by-pixel ratio.
dNDVI	Calculates the difference in NDVI values.	Two images with the same spatial extent.	Data representing the change in NDVI values.
Merge	Allows to copy raster data from a data product to a given data product.	Two or more data products.	A data products containing the combined data from the input data products.
Delete Noise	Removes unwanted noise or artifacts from data.	A data product containing noise or unwanted artifacts	A cleaned data product with reduced noise or artifacts.

ancillary band which produces a basic pixel classification map of L2A data is also applied. Specifically, it is applied to mask pixels not belonging to vegetated natural surfaces (in particular cloud, cloud shadows, water and snow), before computing the NDVI in the subsequent *MS Detection* phase (for which we provide additional details later in this section), by using the channels 4 and 8, centered at 0.665 and 0.842 μm respectively. Then, $S1_{T0}$, $S2_{T0}$ and CLC data are respectively coregistered. Finally, in the *Combined detection* phase, all input data (which we intuitively denote as σ^0_{VV-T0}, σ^0_{VV-T1}, σ^0_{VH-T0}, σ^0_{VH-T1}, $NDVI_{T0}$, $NDVI_{T1}$ and CLC) are coregistered using a nearest neighbour function to upsampling Sentinel-1 and CLC data at the Sentinel-2 spatial resolution, equal to 10m.

We note that, to avoid the requirement of (large) training sets and to favor the automatism of the procedure, we preferred an approach based on the relative variation of σ^0 (at VH and VV pol.) and NDVI rather than supervised machine learning techniques. In particular, the procedure is founded on the hypothesis that the wildfire effects produce a variation of both NDVI and σ^0 over vegetated surfaces (Dindaroglu et al. 2021; Imperatore et al. 2017; Lasaponara and Tucci 2019; Tariq et al. 2021). Such variations can be considered to be due only to strong changes on the natural surfaces (like in the case of wildfires) if the time interval between the satellite acquisition is small enough to avoid other kinds of natural changes, for instance attributable to phenological cycles. Also for this reason 15-days intervals represent a good choice for acquiring images of the SAR and MS image pairs. Finally, the results obtained independently with the optical and microwave remote sensing techniques are combined. As mentioned, for Sentinel-1 images we exploit a method based on the percentage variation of the backscattering coefficient (σ^0) at VH and VV polarizations. Such assumption is founded on experimental observations which assessed SAR backscattering decreases after forest fires because the volume scattering component decreases due to the loss of biomass (Lasaponara and Tucci 2019; Rokhmatuloh et al. 2022). In particular, in the *SAR Detection* phase a pixel is identified as part of burnt surface if the following equations are verified

$$\left(\sigma^0_{VH-T0} - \sigma^0_{VH-T1}\right) > \alpha \cdot \sigma^0_{VH-T0} \tag{1}$$

$$\left|\frac{\sigma^0_{VV-T_0}}{\sigma^0_{VH-T_1}}\right| < \left|\frac{\sigma^0_{VV-T1}}{\sigma^0_{VH-T1}}\right| \tag{2}$$

where σ^0_{VH-T0} and σ^0_{VH-T1} (σ^0_{VV-T0} and σ^0_{VV-T1}) are the corresponding backscattering coefficients at VH polarization of $S1_{T0}$ and $S1_{T1}$, respectively, while α is a threshold value that can be changed to modify the detection sensitivity. In Section "Experimental results", we report the specific value we used in our experimental study.

The above equations are applied to pixels of the SAR image pair over land and where the CLC classes belong to forest cover, agriculture crops and low vegetation. The result is a burnt area map detected by SAR features, in which pixels for which the equations are verified are set to 1 (denoting the burnt surface) and all the other pixels are set to 0.

Regarding Sentinel-2 images, the detection is based on the variation of the NDVI between $S2_{T0}$ and $S2_{T1}$. Specifically, in the *MS Detection* phase, a pixel is classified as part of burnt surface if both the following equations are verified

$$NDVI_{T0} - NDVI_{T1} > \beta \cdot NDVI_{T0} \tag{3}$$

$$NDVI_{T0} - NDVI_{T1} > \gamma \cdot NDVI_{T0} \tag{4}$$

where $NDVI_{T0}$ ($NDVI_{T1}$) is the NDVI value of the corresponding pixel of $S2_{T0}$ ($S2_{T1}$), while β and γ are threshold values that, similarly to α in Eq. 1, can be changed to modify the detection sensitivity. In Section "Experimental results", we discuss the specific values we used also for these thresholds. We note that as an alternative to NDVI, we might use the NBR index. The latter can be calculated using Sentinel-2 Band 8 (NIR) and Band 12 (SWIR), specifically by the equation NBR = (NIR - SWIR) / (NIR + SWIR). The resulting values range from -1 to +1, with lower values indicating more severe burns. However, in our experimental study we did not observed relevant differences when using NDR compared to NDVI. Ultimately, we decided to use NDVI because it is more widely used and NDVI data are more commonly available to users in satellite open data repositories. Moreover, the NDVI based procedure can be applied to data acquired by sensors without the SWIR band.

Equation 3 is applied to pixels belonging to Forest class on the CLC, while Eq. 4 is applied to the other main vegetated surfaces classes. The result of the application of Eqs. 3 and 4 is a burnt area map detected by MS features, in which the pixels for which Eqs. 3 and 4 are verified are flagged as 1 (0 otherwise).

The final burnt area is computed by combining the burnt area maps in the Merge operator, which produces a final map in which a pixel is classified as burnt if at least one of the two corresponding pixels in the input maps is flagged as 1. Finally, the obtained map is post-processed with a feature filter, which is based on pixels clustering and is aimed at deleting small isolated objects with areas smaller than 30 m^2 (i.e. approximately 3 pixels).

We conclude this section with some observations about the approach for selecting the pairs of input images to be processed. Basically, the procedure allows the user to select whichever pair of images. However, we observed that a good approach for implementing long-term continuous surveillance, is the following one. The first Sentinel-2 L2A image (denoted as $S2_{T0}$) is selected as the one with the lowest

cloud cover probability level among the ones available over a 15-day interval. Then, the second Sentinel-2 L2A image (denoted as $S2_{T1}$) is selected as the one with the lowest cloud cover probability level over the following 15 days. Then, the first Sentinel-1 GRD image (denoted as $S1_{T0}$) and the second Sentinel-1 GRD image (denoted as $S2_{T1}$) are selected as the ones with the smallest temporal shift from $S2_{T0}$ and $S2_{T1}$ respectively. For continuous surveillance, the procedure can be applied again to process a set of images taken in the next 15-day intervals, and so on. Overall, since this approach selects images with a lower probability of cloud cover, it improves the accuracy of the results, as we will show later. Furthermore, given the revisit times of Sentinel-1 and Sentinel-2, 15-day intervals ensure that the image pairs are always available.

Implementation details

The data processing workflow is implemented on top of Apache Airflow (Apache 2024), an open-source platform for developing and executing batch-oriented workflows, using Python programming language. Accordingly, the workflow implementation follows the Apache Airflow's DAG specification rules. A detailed file organization is reported in Section "Availability, requirements and software files".

As already mentioned in Section "Procedure design", some workflow steps exploits operators provided by ESA SNAP GPT. These are called via the SNAP Java API through the *esa-snappy* plugin (ESA 2024b). The other workflow steps are entirely implemented in Python language. Thanks to the Airflow task schedule engine, at run-time the executions of the workflow steps can be automatically parallelized and optimized based on the available computing resources of the machine on which the workflow runs. This allows to automatically adapt and optimize the workflow execution depending on the computing resources offered by the virtual machine (VM) the workflow is running on. Ultimately, this enables the users to select, based on their needs, the types of VMs among the ones provided by the cloud platform. To automate the configuration and the execution of the workflow on a VM, we created a dedicated Docker container (Docker 2024) which includes the workflow implementation and all information on software requirements (Airflow, ESA SNAP GPT, esa-snappy, other libraries, etc.). The container is included in a VM image, which is selected when the VM is created, and is activated when the VM is started, so as the installation of all the required software packages can be automatically performed.

For our experimental study, to increase the automation level in the execution of the procedure on the cloud platform, we implemented a script that allows to run one or multiple workflow instances in parallel, each one taking in input a different set of images. Specifically, it creates a VM for each set of images to be processed, then, in each VM, it uploads a set of input images, taking them from the cloud provider's image storage system, and executes the workflows. We note that the API provided by many public cloud platforms allows to easy implement this kind of scripts, and this facilitates the execution of the procedure to analyze extended geographic area (which can require to process many sets of input images), or extended time intervals (which can require to process many temporally subsequent couples of images of the same area). Noteworthy, this improves the scalability of the procedure, thanks to the automatic exploitation of multiple VMs in parallel based on the area size and the length of the time interval to analyze.

Experimental results

In this section, we present the results of an experimental study related to three large wildfire events occurred over the recent years in different countries. They occurred in Sardinia (Italy, July 2021), in Covilhã (Portugal, August 2022) and in Rhodes Island (Greece, July 2023), respectively. As mentioned, the results provided by the procedure were evaluated using EFFIS data as a reference.

For each test case, we evaluated the set of metrics listed in Table 2. Accuracy provides an overall measure of correct classifications. However, it can be misleading in imbalanced datasets (where burned area is much smaller than unburned area). Therefore, metrics like precision and recall are essential. Precision measures the fraction of correctly identified burned pixels among all pixels classified as burned, minimizing false positives. Recall, also known as sensitivity, measures the proportion of correctly identified burned pixels among all actual burned pixels the over the scene, minimizing false negatives. In burn detection, minimizing false negatives (missing actual burns) is often prioritized, making recall particularly important. Specificity measures the proportion of correctly identified unburned pixels among all actual unburned pixels. The F1-score, the harmonic mean of precision and recall, provides a balanced measure when both minimizing false positives and false negatives is important. False Positive Rate and False Negative Rate directly quantify the proportions of these errors. Negative Predictive Value measures the proportion of correctly identified unburned pixels among all pixels classified as unburned. The fraction of incorrect negative predictions and fraction of incorrect positive predictions are simply a different formulation of the false negative and positive rates, respectively and therefore do not provide additional information. To further assess the spatial accuracy of the detected burn perimeters, the Intersection over Union (IoU), also known as the Jaccard Index, mea-

Table 2 Metrics estimated for all test cases

Metric	Calculated as (Acronyms are specified below)
Specificity (Sp)	$TN/(TN+FP)$
Recall (Re)	$TP/(TP+FN)$
False Negative Rate	$FN/(TP+FN)$
False Positive Rate	$FP/(TN+FP)$
Negative Predictive Value	$TN/(TN+FN)$
Precision	$TP/(TP+FP)$
Fraction of Incorrect Negative Predictions	$FN/(TN+FN)$
Fraction of Incorrect Positive Predictions	$FP/(TP+FP)$
Accuracy	$(TP+TN)/(TP+TN+FP+FN)$
F1 Score (Knopp et al. 2020)	$(2 \cdot Pr \cdot Re)/(Pr+Re)$
Intersection over Union (IoU)	$TP/(TP+FP+FN)$
Dice Coefficient	$(2 \cdot TP)/(2 \cdot TP+FP+FN)$
where:	
TP is the number of True Positive samples (number of times the model correctly classified a sample as positive)	
TN is the number of True Negative samples (number of times the model correctly classified a sample as negative)	
FP is the number of False Positive samples (number of times the model incorrectly classified a sample as positive)	
FN is the number of False Negative samples (number of times the model incorrectly classified a sample as negative)	

sures the overlap between predicted and actual burned areas, providing a crucial measure of spatial agreement. The Dice Coefficient, offers a similar measure of spatial overlap, less sensitive to large differences in area size. For each test case, we will also report confidence intervals to provide a measure of uncertainty in the accuracy estimation. The Kappa coefficient (Cohen 1960) offers a measure of agreement corrected for chance, providing a more robust assessment than raw accuracy, especially in imbalanced datasets. All the above metrics, in conjunction with accuracy, can provide a comprehensive understanding of a burn detection method's performance, particularly its ability to correctly identify both burned and unburned areas, and their spatial extent and severity.

To the aim of our experimental evaluation, EFFIS products were coregistered with the burn maps provided by the procedure, matching their spatial resolution equal to 10m.

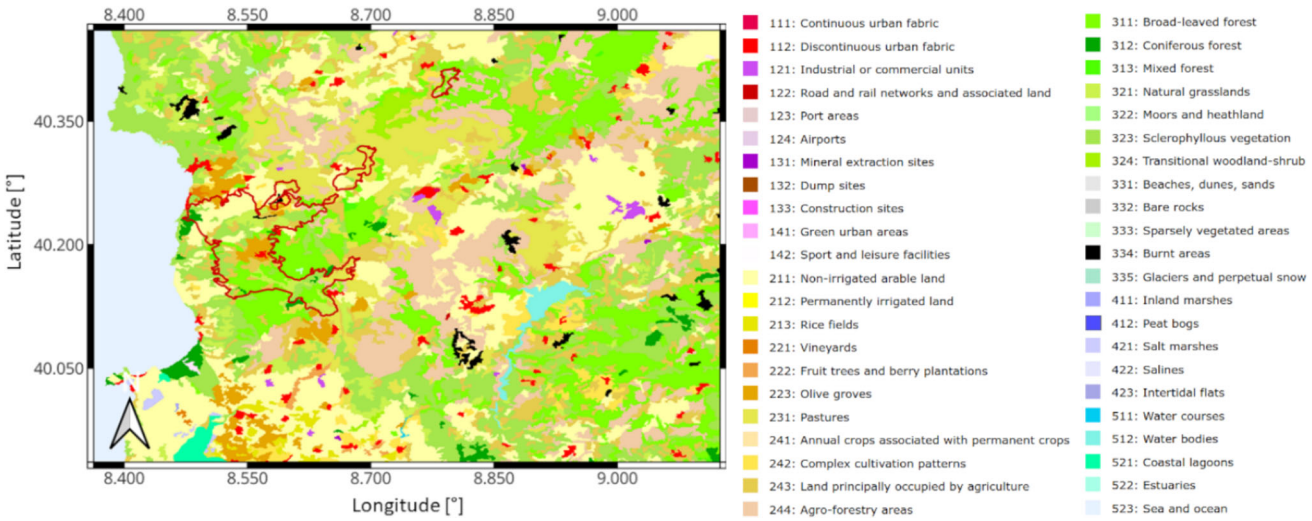

Fig. 2 Burnt area perimeter for the first test case detected by EFFIS (red polyline) over the CLC 2018 classification map of the area of interest

Table 3 Dates of the input images used for the first test case

Input images	Acquisition Dates
$S1_{T0}$	12 July 2021 (Asc.)
$S1_{T1}$	30 July 2021 (Asc.)
$S2_{T0}$	10 July 2021
$S2_{T1}$	30 July 2021

Regarding parameters α, β and γ in Eqs. 1, 3 and 4 of Section "Procedure design", after exploring various configurations, we set $\alpha = 0.25$, $\beta = 0.3$ and $\gamma = 0.5$, since we found that such a combination of values provided on average good results over all test cases.

Since we used AWS-EC2 as a cloud platform, which offers a variety of VM types, we also collected as set of data related to the execution of the workflow on different VM types. In particular, we measured the workflow execution times and the VM usage costs (calculated by multiplying the VM usage time and the resource prices per time unit, as reported by the cloud provider's resource price list). These data, that we report in Appendix A, can provide the reader with interesting performance metrics about the procedure.

First test case: Sardinia wildfires (July 24, 2021)

The first test case concerns a wildfire event occurred on July 24, 2023 around Oristano, western Sardinia. The lower left corner and upper right corner of the considered area are (39.9517°N; 8.4374°E) and (40.4735°N; 8.9156°E), respectively. The estimated burnt area is equal to 11,073.2 ha. In Fig. 2, the detected burnt area perimeter by EFFIS (activation code EMSR523) is depicted on top of the CLC 2018 map, showing that the fire interested different natural surfaces, including agriculture crops, such as non-irrigated arable land and vineyards, forest areas and natural grassland. Data used as input to the procedure in this test case are specified in Table 3. Figure 3 shows the σ^0 at VH polarization of the Sentinel-1 and the Near Infrared color composite (obtained applying the following bands association R: band-8 (842 nm), G: band-4 (665 nm), B: band-3 (560 nm)) of the Sentinel-2 input images.

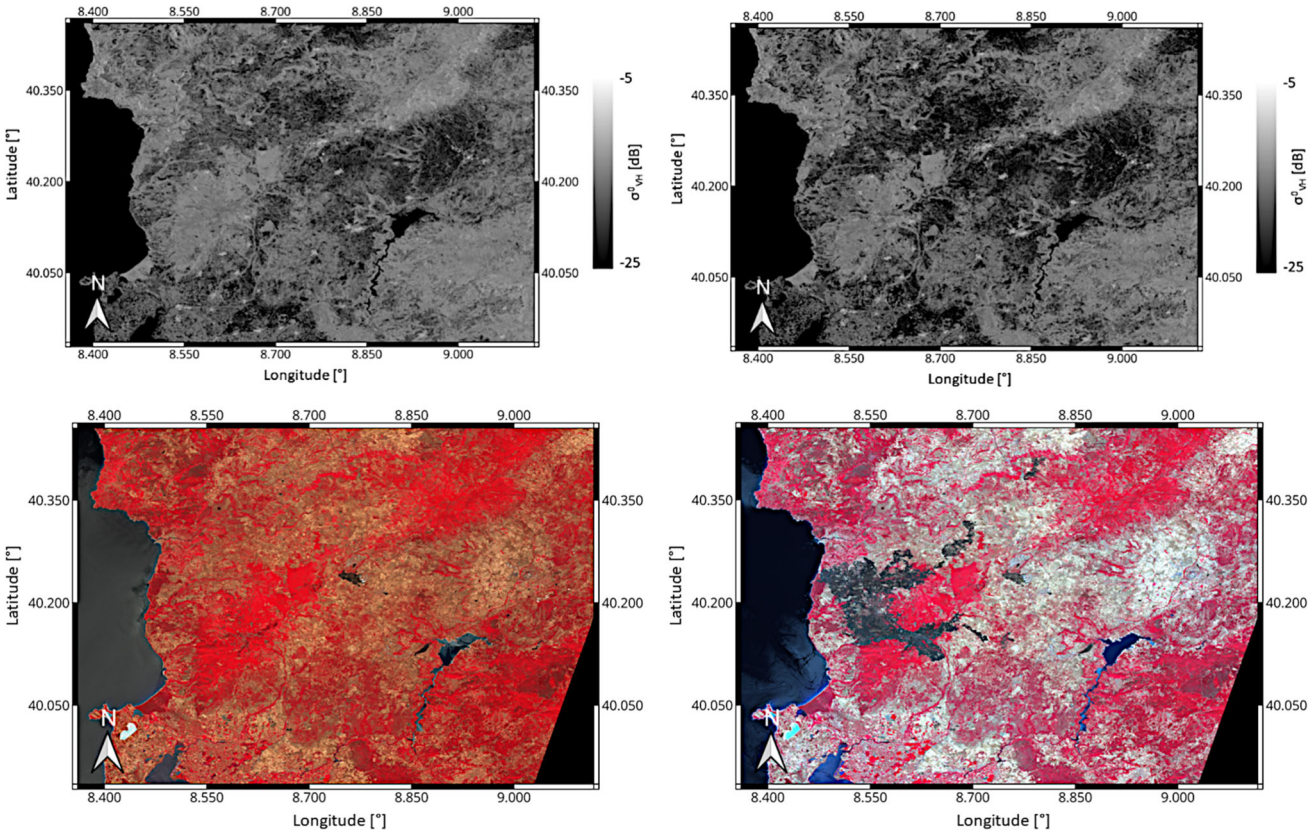

Fig. 3 Input data used by the procedure for the first test case. Top plate: $S1_{T0}$ Radar Backscattering image (σ^0) at VH polarization (left) and $S1_{T1}$ Radar Backscattering image (σ^0) at VH polarization (right). Bottom plate: Near Infrared color composite of $S2_{T0}$ image (left) and Near Infrared color composite of $S2_{T1}$ image (right)

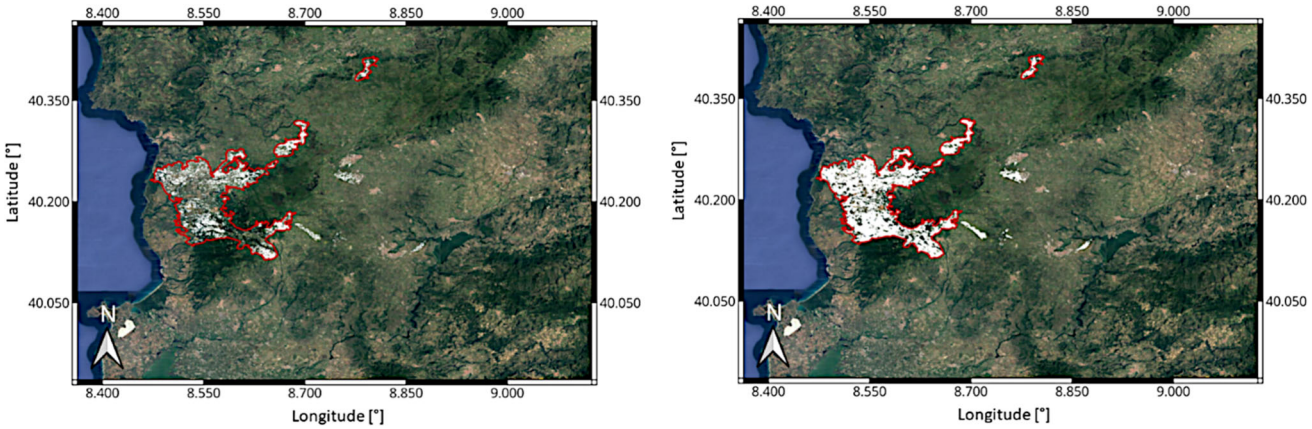

Fig. 4 Map of burnt area (evidenced by white pixels) detected by the *SAR Detection* phase (left) and by the *MS Detection* phase (right) of the procedure

Figure 4 shows the two burnt areas identified by the *SAR Detection* phase of the procedure (thus using only Sentinel-1 data, left image) and by the *MS Detection* phase of the procedure (thus using only Sentinel-2 data, right image), respectively. The area detected by the *SAR Detection* phase is shown over the Natural color composite (R: band-4 (665 nm), G: band-3 (560 nm), B: band-2 (490 nm)) of $S2_{T1}$. The final burnt area detected by the procedure is shown in Fig. 5 (left image), together with the burnt area reported by EFFIS (right image). We considered the most recent and consolidated burnt severity map produced during the EFFIS EMSR523 activation procedure. For this EFFIS activation Sentinel-2 products, whit a GSD equal to 10m, were used. In particular, the Pre-event image was acquired by Sentinel-2A on the 12 of July 2021 at 10:10 UTC (with a cloud coverage in AoI approximatively equal to 0%). The Post-event image was acquired by Sentinel-2A on the 27 of July 2021 at 10:05 UTC (with a cloud coverage in AoI approximatively equal to 35%). In order to rescale the EFFIS burnt severity map on the 0-1 range used by the burnt map produced by our procedure, the pixels of the EFFIS map with burnt severity ≥ 1 are set equal to 1, while all the other pixels equal to 0. In the figure the pixels identified as burnt area by the procedure are shown in cyan, while the "burnt" pixels derived by EFFIS data are shown in orange. On the maps, the contours of the wildfire footprint as identified by EFFIS data are depicted with red polylines for visualization purposes.

Table 4 shows the values of the evaluation metrics calculated by considering the EFFIS map pixels having burnt severity ≥ 1 , thus comparing burnt and unburnt pixels identified by the procedure and by the EFFIS map. Specifically, the table reports the values of the metrics obtained by considering the final burnt area detected by the procedure (i.e. the one estimated through the combined detection), the one

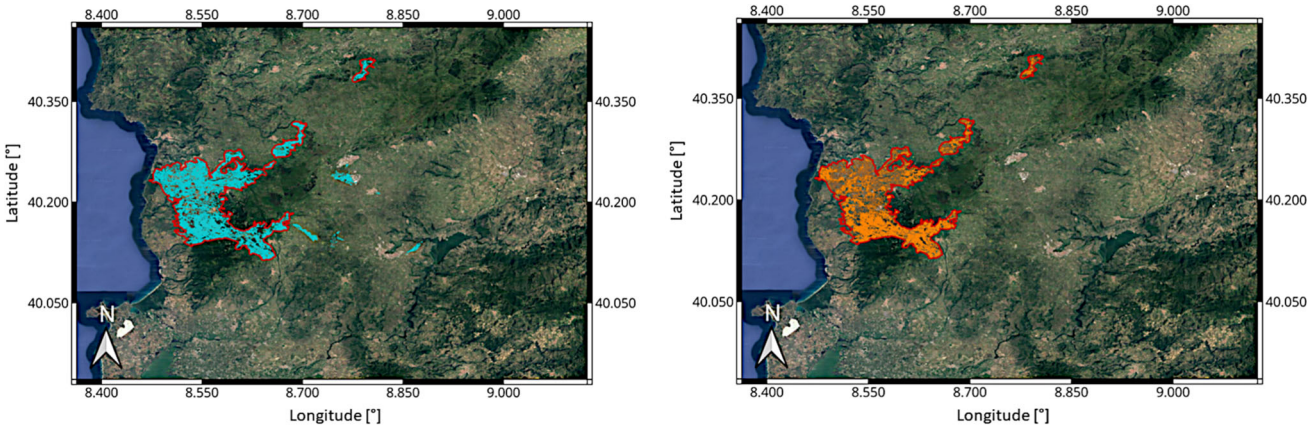

Fig. 5 Maps of burnt area of the first test case superimposed to the Google satellite basemap. Left image: Map of burnt area detection (evidenced by cyan pixels) obtained by the procedure. Right image: Map of the burnt area (evidenced by orange pixels) obtained by thresholding the burnt severity map produced by EFFIS for the EMSR523 activation. On both maps, the contours of the wildfire footprint produced by EFFIS are reported by red polylines

Table 4 Values of the metrics obtained for the first test case using the different combinations of Sentinel data, and using EFFIS products for comparison

Metric	Procedure Outputs		
	Combined Detection	SAR Detection	MS Detection
Specificity	88%	92%	82%
Recall	86%	42%	79%
False Positive Rate	12%	08%	18%
False Negative Rate	14%	58%	21%
Negative Predictive Value	86%	61%	80%
Precision	88%	83%	81%
Fraction of Incorrect Negative Predictions	14%	39%	20%
Fraction of Incorrect Positive Predictions	12%	17%	19%
Accuracy	0.868	0.669	0.803
F1 Score	0.867	0.600	0.801
IoU	0.810	0.458	0.758
Dice Coefficient	0.882	0.633	0.862
k Coefficient	0.855	0.550	0.802

Note: The 95% confidence intervals associated to Accuracy with Sentinel-1 and Sentinel-2 are 0.858 and 0.878, respectively

detected by the *SAR Detection* phase and the one detected by the *MS Detection* phase. We note that the procedure detected some burnt areas not included in the EFFIS map. This can be due to the different footprint and acquisition dates of the satellite data used by EFFIS with respect to our procedure. Indeed, the burnt severity map of EFFIS is obtained on the basis of Pléiades-1 products at the post event date 28 of July 2021, so two days before the acquisition date of the $S1_{T1}$ and $S2_{T1}$ images used by the procedure. Due to this aspect, since the evaluation metrics reported in Table 4 are estimated in comparison with the EFFIS map, the accuracy of the procedure is affected by the increase of the FPR caused by the additional burnt areas detected.

In summary, the values of the evaluation metrics show that the results based only on Sentinel-2 data are overall better than those based only on Sentinel-1 data, as expected. However, with the combined detection, Accuracy and F1 Score are significantly higher, as well as better results are achieved with most of the other metrics, demonstrating the improvement by exploiting both SAR and MS data.

Second test case: Covilhã wildfires (August, 8 2022)

The second test case refers to a wildfire occurred on 8 August 2022 around Covilhã, Portugal. The lower left corner and the upper right corner of the considered areas are

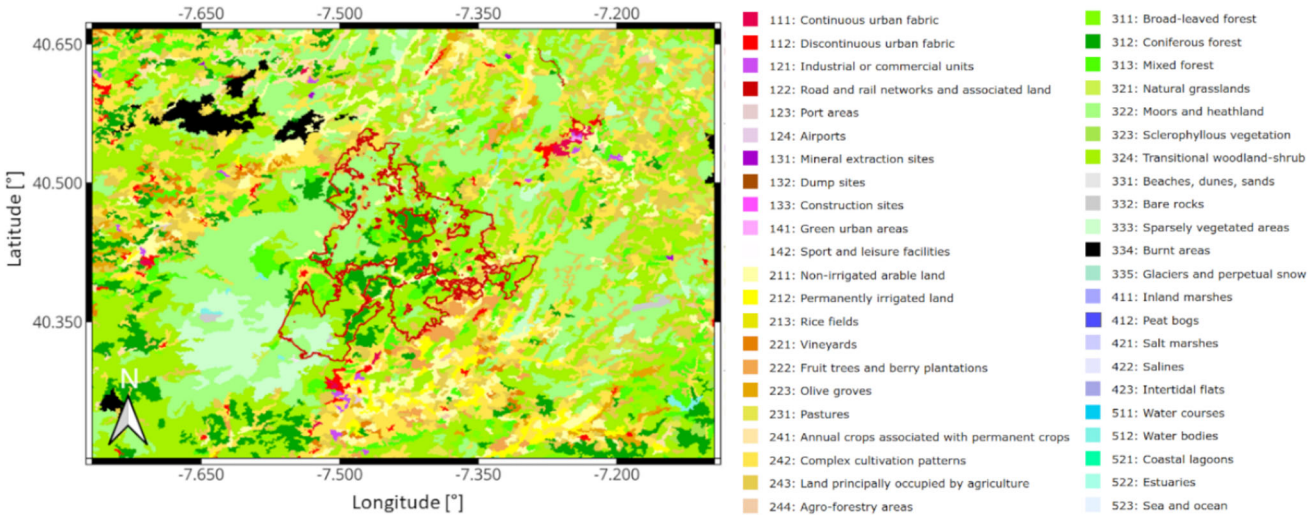

Fig. 6 Burnt area perimeter for the second test case as detected by EFFIS (red polyline) over the CLC 2018 classification map of the area of interest

Table 5 Dates of the input images used for the second test case

Input images	Acquisition Dates
$S1_{T0}$	29 July 2022 (Asc.)
$S1_{T1}$	22 August 2022 (Asc.)
$S2_{T0}$	02 August 2022
$S2_{T1}$	22 August 2022

(40.2249°N; 7.705°W) and (40.6444°N; 7.1574°W), respectively. The detected burnt area reported by EFFIS (activation code EMSR618) is equal to 24,938.9 ha, and is reported in Fig. 6 on the CLC 2018 map. For this EFFIS activation, AIRBUS SPOT6 and SPOT7 products, with a GSD equal to 1.5m, were used. In particular, the Pre-event image was acquired by SPOT6 on the 28 of May 2022 at 11:00 UTC (with a cloud coverage in AoI approximatively equal to 0% and 15.3°off-nadir angle). The Post-event image was acquired by SPOT7 on the 18 of August 2022 at 10:29 UTC (with a cloud coverage in AoI approximatively equal to 0% and 37.6°off-nadir angle). As shown, the wildfire interested vegetated surfaces, mainly characterized by natural grassland, transitional woodland-shrub, mixed and coniferous forests. The CLC map also shows some burnt areas due to wildfires prior to the event occurred on 8 August 2022 and before the release of the 2018 CLC classified map.

Input data used by the procedure for the second test case are reported in Table 5. The σ^0 at VH polarization of $S1_{T0}$ and $S1_{T1}$, together with the Near Infrared color composite of $S2_{T0}$ and $S2_{T2}$, are shown in Fig. 7. Figure 8 shows the two burnt areas identified by the *SAR Detection* phase (left image) and by the *MS Detection* phase (right image). Finally, Fig. 9 depicts the final area detected by the procedure (left image) and the one provided by EFFIS (right image). Again, we used the most recent and consolidated map released at the closure of the EFFIS EMSR618 activation procedure.

Table 6 reports the values of the metrics we obtained by comparing the burnt areas detected by the procedure and by the EFFIS map pixels, evaluated as for the first test case. As shown by the data, also with this test case the combined use of SAR and MS data provided the highest values for Accuracy, F1 Score and for many of the other metrics. The SAR signal is less sensitive than the MS one over some areas, producing a low rate of burnt area detection with respect to

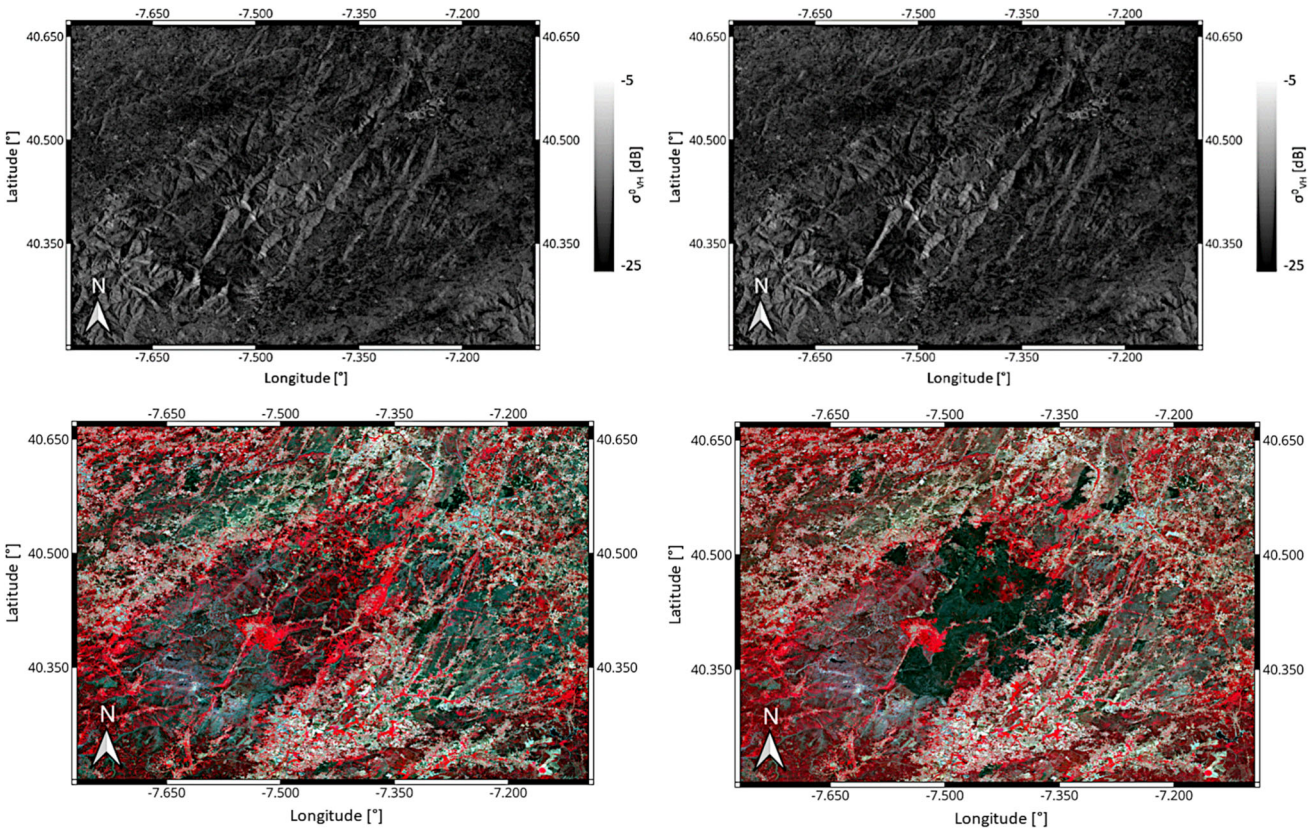

Fig. 7 Input data used by the procedure for the second test case. Top plate: $S1_{T0}$ Radar Backscattering image (σ^0) at VH polarization (left) and $S1_{T1}$ Radar Backscattering image (σ^0) at VH polarization (right). Bottom plate: Near Infrared color composite of $S2_{T0}$ image (left) and Near Infrared color composite of $S2_{T1}$ image (right)

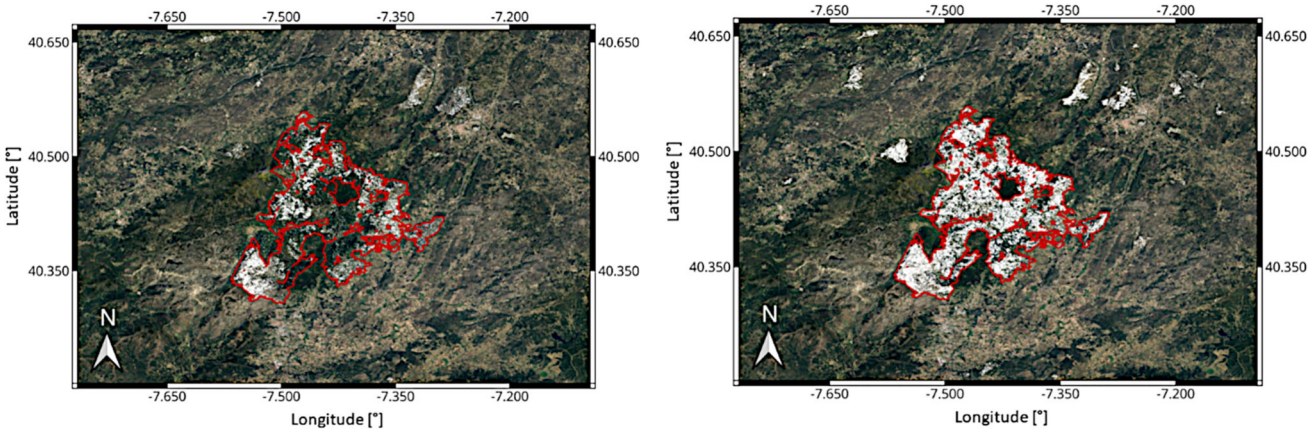

Fig. 8 Map of burnt area (evidenced by white pixels) detected by the *SAR Detection* phase (left) and by the *MS Detection* phase (right) of the procedure

EFFIS data. However, such a behavior influences the high accuracy achieved on the side of not burnt pixels.

With this test case we highlight another advantage of our procedure, in particular when used for automatic surveillance, provided by the combined use of SAR and MS data. Sometimes MS data are unusable due to, for example, the presence of meteorological clouds or fire's smoke during the burning phase. Note that these phenomena may last for several days and thus may affect one or more subsequent Sentinel-2 acquisitions. Therefore, in these cases, SAR data would be the only available source to detect fires in areas not visible in the MS images. In our test case, this would happen if $S2_{T1}$ was acquired on 7 August 2022. Indeed, as its color composite in Fig. 10 (top right image) shows, a column of smoke appears. In this type of situations, the procedure still allows for early burn detection on the area covered by the smoke column by using Sentinel-1 data (which we show in Fig. 10, top left image, acquired on 8 August 2022). From the output of the *SAR Detection* phase (reported in Fig. 10, bottom image) it is possible to note that it detected burnt areas in correspondence to the smoke column, in particular close its origin, where it the smoke is more intense.

Third test case: Island of Rhodes wildfires (July 18, 2023)

The third test case refers to a wildfire occurred on July 18, 2023 on the Greek island of Rhodes. The lower left corner and upper right corner of the considered areas are (35.9484°N; 27.7065°E) and (36.3258°N; 28.1986°E), respectively. The detected burnt area identified by EFFIS (activation code EMSR675) is equal to 17628.7 ha, and is shown in Fig. 11 on the CLC 2018 map. The map highlights as the wildfire interested mainly natural vegetated surfaces, mostly characterized

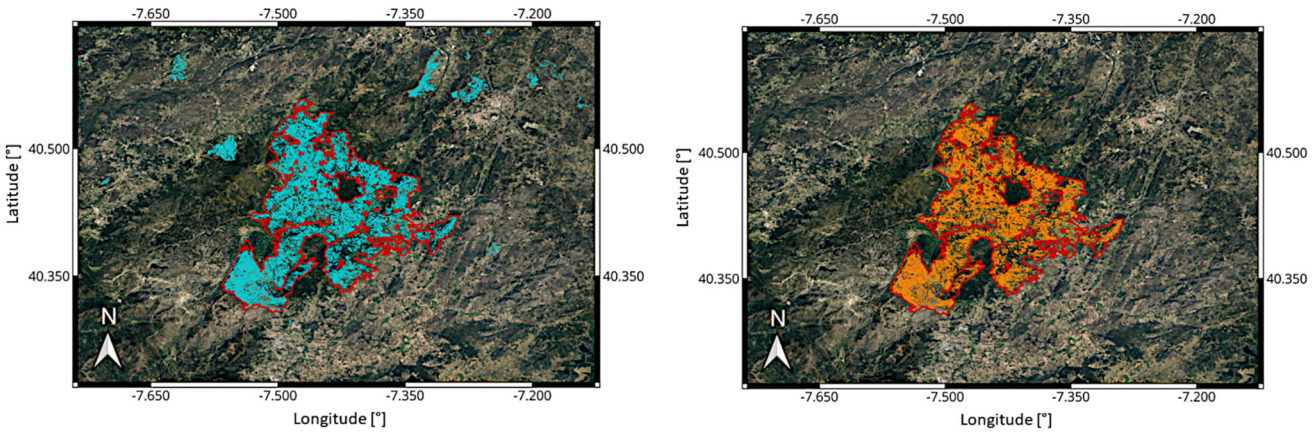

Fig. 9 Maps of burnt area of the second test case superimposed to the Google satellite basemap. Left image: Map of burnt area detection (evidenced by cyan pixels) obtained by the procedure. Right image: Map of the burnt area (evidenced by orange pixels) obtained by thresholding the burnt severity map produced by EFFIS for the EMSR618 activation. On both maps, the contours of the wildfire footprint produced by EFFIS are reported by red polylines

Table 6 Values of the metrics obtained for the second test case using the different combinations of Sentinel data, and using EFFIS products for comparison

Metric	Procedure Outputs		
	Combined Detection	SAR Detection	MS Detection
Specificity	94%	96%	92%
Recall	86%	40%	84%
False Positive Rate	02%	04%	08%
False Negative Rate	14%	60%	16%
Negative Predictive Value	87%	61%	85%
Precision	93%	90%	91%
Fraction of Incorrect Negative Predictions	13%	39%	15%
Fraction of Incorrect Positive Predictions	07%	10%	09%
Accuracy	0.894	0.708	0.878
F1 Score	0.890	0.645	0.876
IoU	0.834	0.472	0.783
Dice Coefficient	0.862	0.614	0.854
k Coefficient	0.837	0.528	0.804

Note: The 95% confidence intervals associated to Accuracy with Sentinel-1 and Sentinel-2 are 0.839 and 0.917, respectively

by grassland and coniferous forests, and some agriculture areas. For this EFFIS activation, Planet PlanetScope products, whit a GSD equal to 3m, were used. In particular, the Pre-event image was acquired on the 17 of July 2023 at 8:34

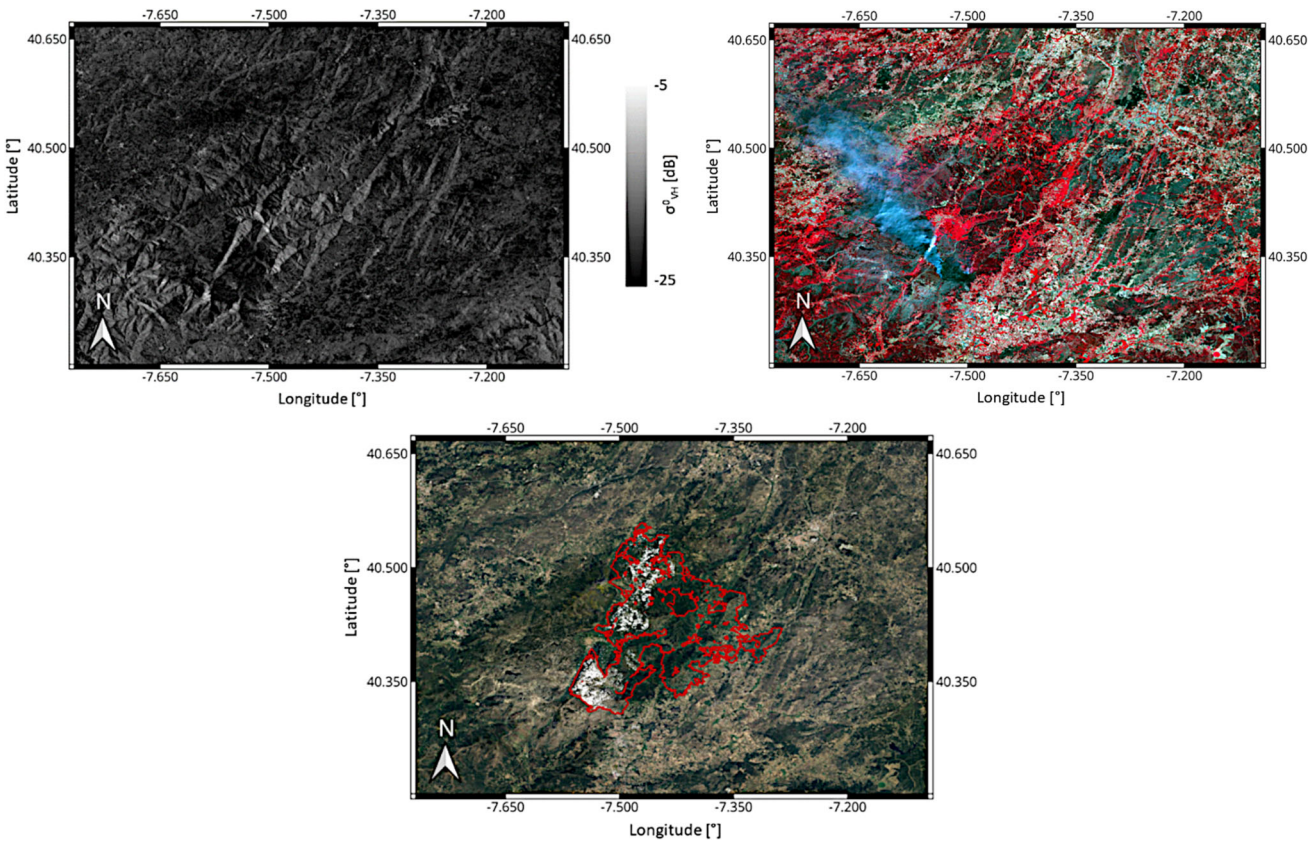

Fig. 10 Top plate: $S1_{T1}$ Radar Backscattering image (σ^0) at VH polarization (left) and Near Infrared color composite of $S2_{T1}$ image (right) acquired on 7 August 2022 and acquired on 8 August 2022, respectively. Bottom plate: Map of burnt area (evidenced with white pixels) detected by the *SAR Detection* phase

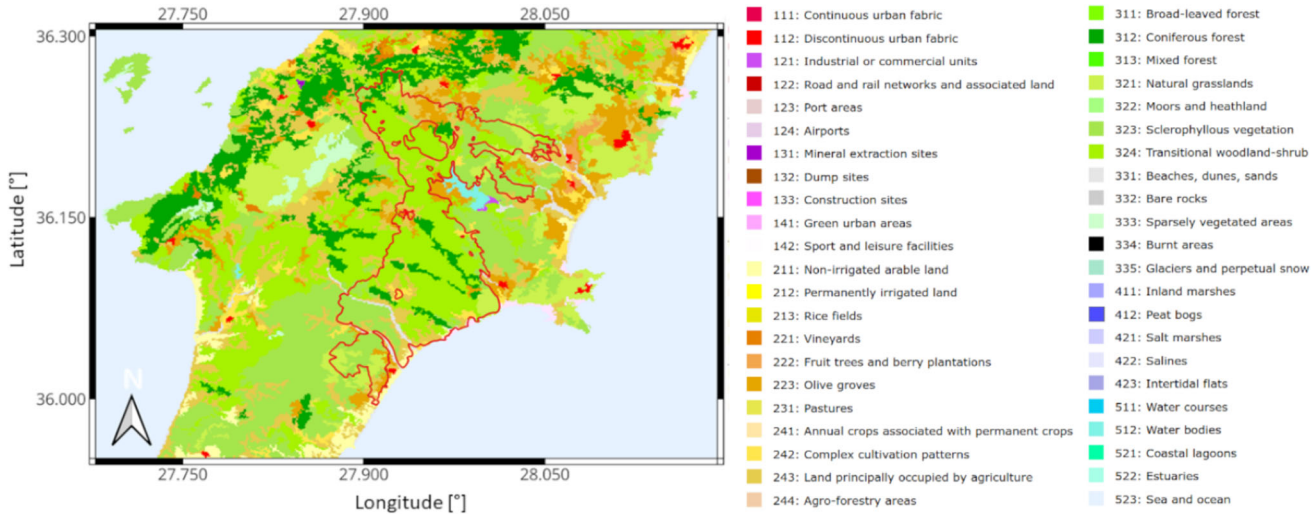

Fig. 11 Burnt area perimeter for the third test case as detected by EFFIS (red polyline) over the CLC 2018 classification map of the area of interest

UTC (with a cloud coverage in AoI approximatively equal to 0%). The Post-event image was acquired on the 17 of July 2023 at 8:36 UTC (with a cloud coverage in AoI approximatively equal to 0%).

Input data for the procedure are reported in Table 7. Figure 12 shows the true color composite of the Sentinel-2 images and the σ^0 at VH polarization of the Sentinel-1 images. Figure 13 shows the two burnt areas identified by the *SAR Detection* phase (left image) and by the *MS Detection* phase (right image). Figure 14 shows the final burnt area detected by our procedure (left image) and by EFFIS (right image), still using the most recent and consolidated map produced during the EFFIS EMSR675 activation procedure. The values of the evaluation metrics are reported in Table 8. Again, they confirm that the results obtained using the combination of MS and SAR data provides the highest values for both accuracy and F1 score, and for most of the other metrics.

Discussion

In all the test cases presented in Section "Experimental results", the procedure with the combination of both MS and SAR data provided the best overall performance with respect to the balancing between the determination of correct burnt and unburnt pixels in the area of the fire occurrence, as delimitated by EFFIS data. As expected, the results based only on the Sentinel-2 data report a better agreement with the EFFIS burnt area maps, since the latter comes from optical images as well. This confirms the validity of the proposed simplified method based on two thresholds applied to the NDVI variation recorded between two data, acquired before and after the event respectively. Indeed, we assessed how the pixels, for which the MS spectral index is influenced by fire, are in general well identified, regardless of the specific land cover of the affected areas. As expected with the Sentinel-1 products, the behavior of the backscattering coefficient variations with respect to fire effects and surface conditions is more complex, and it depends on the type of surface affected by fire and on the burnt severity. Moreover, to limit additional effects on the radar backscattering, we avoided test cases characterized by steep topography. This allowed us to consider Sentinel-1 images acquired only by ascending orbits. With a view of applying the procedure to all the possible cases of wildfires, therefore including forest fires in mountain areas, a variation of the proposed approach can be formulated considering both ascending and descending orbits and applying the masking of layover and shadows areas. Anyway, it is important to note that the usage of the Sentinel-1 data alone produces still acceptable values of accuracy, which allows to consider the possibility to perform burnt area detection with SAR data when MS observations are influenced by meteorological clouds or smoke. To assess the possible causes of the SAR detection errors, we conducted a further analysis with respect to the CLC 2018 products. In particular, we analyzed the pixels identified as burnt by the EFFIS products and not detected by SAR.

The histogram in Fig. 15 reports the occurrences of the SAR misdetections with respect to the surfaces classes

Table 7 Dates of the input images used for the third test case

Input images	Acquisition Dates
$S1_{T0}$	11 July 2023 (Asc.)
$S1_{T1}$	23 July 2023 (Asc.)
$S2_{T0}$	13 July 2023
$S2_{T1}$	28 July 2023

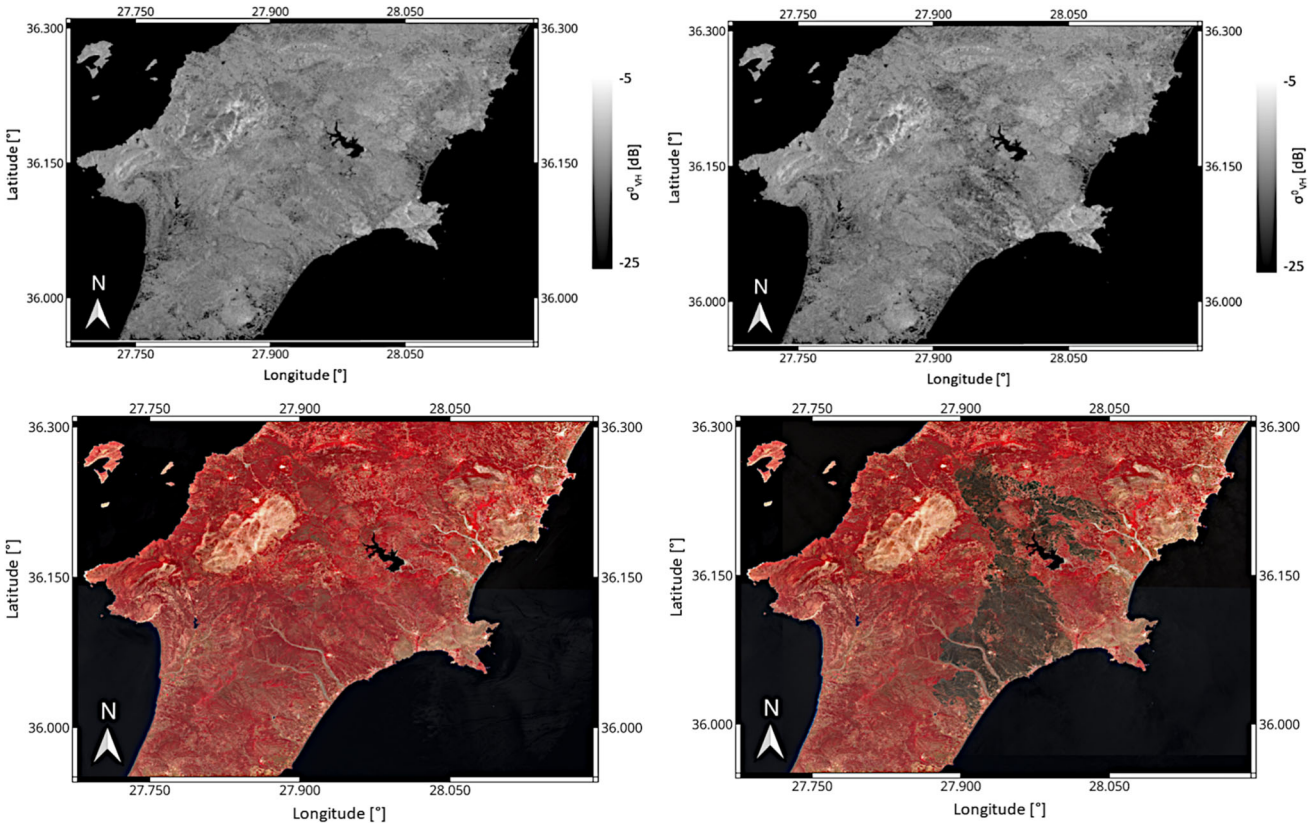

Fig. 12 Input data used by the procedure for the third test case. Top plate: $S1_{T0}$ Radar Backscattering image (σ^0) at VH polarization (left) and $S1_{T1}$ Radar Backscattering image (σ^0) at VH polarization (right). Bottom plate: Near Infrared color composite of $S2_{T0}$ image (left) and Near Infrared color composite of $S2_{T1}$ image (right)

derived from the CLC 2018 product. It shows that for the three considered test cases most of the burnt pixel missed by the procedure using only Sentinel-1 products belongs to natural vegetated surfaces. The CLC 2018 classes which are related to the majority of missing occurrence are: 12 - Non-irrigated arable land, 17 - Olive groves, 18 - Pastures, 21 - Land principally occupied by agriculture with significant areas of natural vegetation, - Agro-forestry areas, 26 - Natural grasslands, and 28 - Sclerophyllous vegetation.

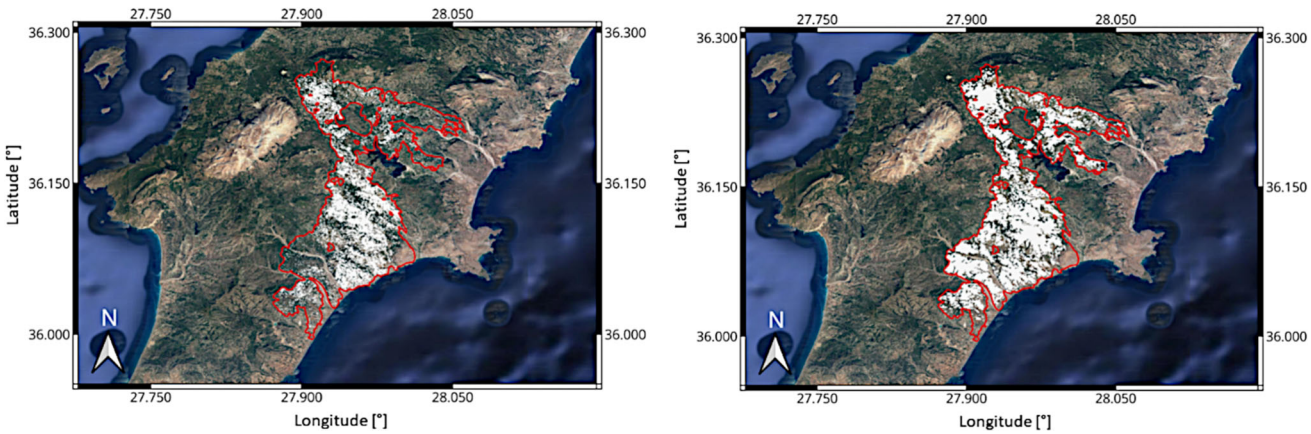

Fig. 13 Map of burnt area (evidenced by white pixels) detected by the *SAR Detection* phase (left) and by the *MS Detection* phase (right) of the procedure

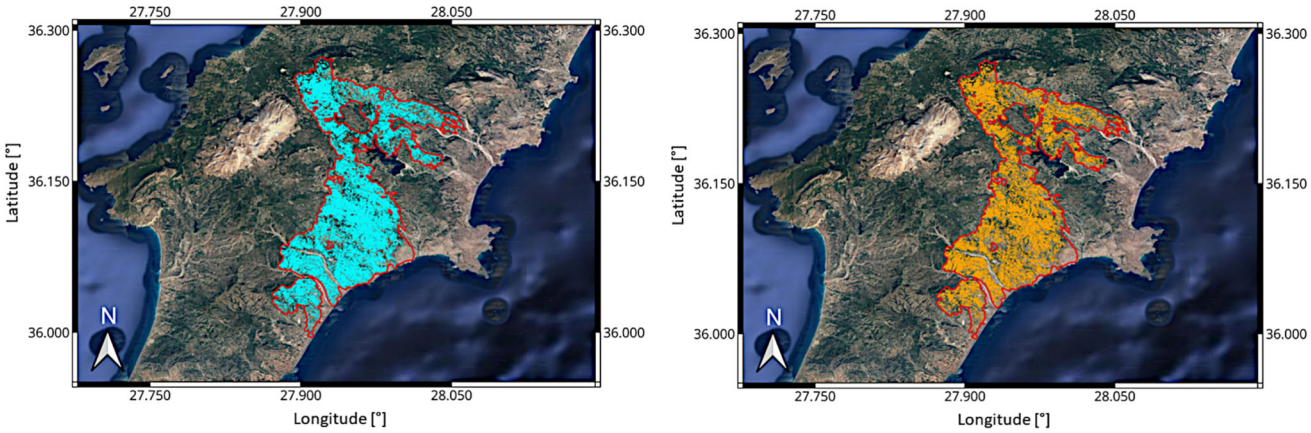

Fig. 14 Maps of burnt area of the third test case superimposed to the Google satellite basemap. Left image: Map of burnt area detection (evidenced by cyan pixels) obtained by the procedure. Right image: Map of the burnt area (evidenced by orange pixels) obtained by thresholding the burnt severity map produced by EFFIS for the EMSR675 activation. On both maps, the contours of the wildfire footprint produced by EFFIS are reported by red polylines

Some minor missing errors are referred to the CLC classes 23 and 24, respectively, identifying Broad-leaved forest and Coniferous forest. Those results highlight a certain weakness of the approach based on the percentage variation of the backscattering coefficient, and the increasing of the polarization ratio to detect fire effects on challenging classes characterized in general by low to moderate vegetation coverage for which the diffuse volume scattering may not be the predominant scattering mechanism.

Anyway, it is important to note that the usage of the Sentinel-1 data alone produces significant values of Precision and Specificity which support a valuable discrimination between burnt and non-burnt areas with SAR data

Conclusions

This article presented the design and the evaluation study of a procedure based on the combination of SAR and MS data to detect burnt areas over vegetated natural surfaces. The underpinning workflow is based on the variation of NDVI and σ^0 at VH polarization as recorded on pairs of images collected before and after a wildfire. The experimental results achieved with three large fire events reported an overall accuracy, evaluated thorough EFFIS data, greater than 0.86. Overall, they showed that the proposed approach has significant potential for creating tools for fire monitoring. Ultimately, since the proposed solution can be easily implemented and operated by anyone by exploiting public cloud computing services

Table 8 Values of the metrics obtained for the third test case using the different combinations of Sentinel data, and using EFFIS products for comparison

Metric	Procedure Outputs		
	Combined Detection	SAR Detection	MS Detection
Specificity	92%	89%	93%
Recall	87%	53%	83%
False Positive Rate	08%	11%	07%
False Negative Rate	13%	47%	17%
Negative Predictive Value	87%	65%	83%
Precision	92%	82%	93%
Fraction of Incorrect Negative Predictions	13%	35%	17%
Fraction of Incorrect Positive Predictions	08%	18%	07%
Accuracy	0.901	0.677	0.8767
F1 Score	0.895	0.551	0.870
IoU	0.813	0.484	0.787
Dice Coefficient	0.891	0.643	0.882
k Coefficient	0.887	0.658	0.877

Note: The 95% confidence intervals associated to Accuracy with Sentinel-1 and Sentinel-2 are 0.894 and 0.912, respectively

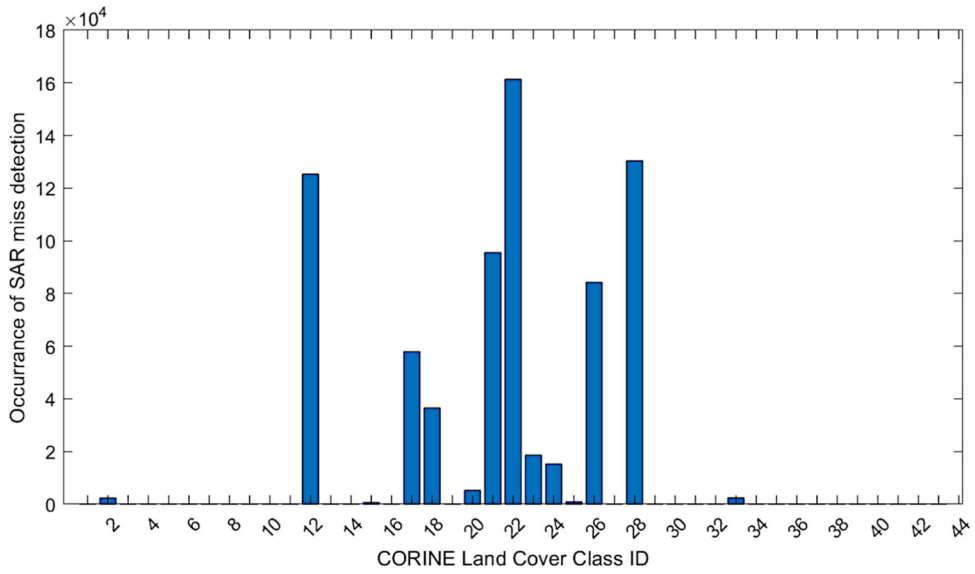

Fig. 15 Histogram of the CLC 2018 classes category, extracted by evaluating the miss classified burnt pixels of the SAR based burn detection map for which the EFFIS products of the three considered test cases report a burn severity ≥ 1

and open data, we believe that the results of this study can be useful to the community of Earth observation researchers and software designers.

Availability, requirements and software files

An open source implementation of the workflow is available at the repository https://github.com/bitwiseops/fire-detection. The repository also includes the Dockerfile to automatize the creation of the Docker image. Requirements for running the workflow are the following ones:

- Hardware: 32 GB RAM, 128 GB HDD (recommended)
- Software:
  - Python3 Interpreter (https://python.org)
  - Apache Airflow (https://airflow.apache.org)
  - ESA SNAP (https://step.esa.int/main/download/snap-download)

The software structure includes the following files and folders:

- *s1_s2_fire_detection.py*, a file that contains the workflow declaration according to Apache Airflow's DAG declaration rules
- *operators*, a folder that contains the following files implementing various operators used by the workflow:
  - *gpf.py*
  - *net.py*
  - *raster.py*

Appendix A: Performance and operation cost data in cloud

Table 9 and Fig. 16 of this appendix show some performance and operation cost data collected during the experi-

Table 9 Average execution times and costs for different VM type on AWS EC2

VM type	Expected execution time (min)	Cost ($)
c5.4xlarge	58.20	0.93
c5.9xlarge	44.50	1.43
c5.12xlarge	39.30	1.64
c5.18xlarge	36.20	2.22
c5.24xlarge	35.10	2.83
m5.4xlarge	49.40	0.91
m5.8xlarge	42.10	1.42
m5.12xlarge	37.10	1.82
m5.16xlarge	34.10	2.20
m5.24xlarge	32.00	3.04
c7i.4xlarge	59.00	0.98
c7i.8xlarge	49.50	1.50
c7i.12xlarge	44.20	1.94
c7i.16xlarge	40.50	2.33
c7i.24xlarge	37.20	3.14
m7i.4xlarge	51.50	0.99
m7i.8xlarge	40.40	1.42
m7i.12xlarge	34.20	1.76
m7i.16xlarge	29.50	2.00
m7i.24xlarge	25.50	2.54

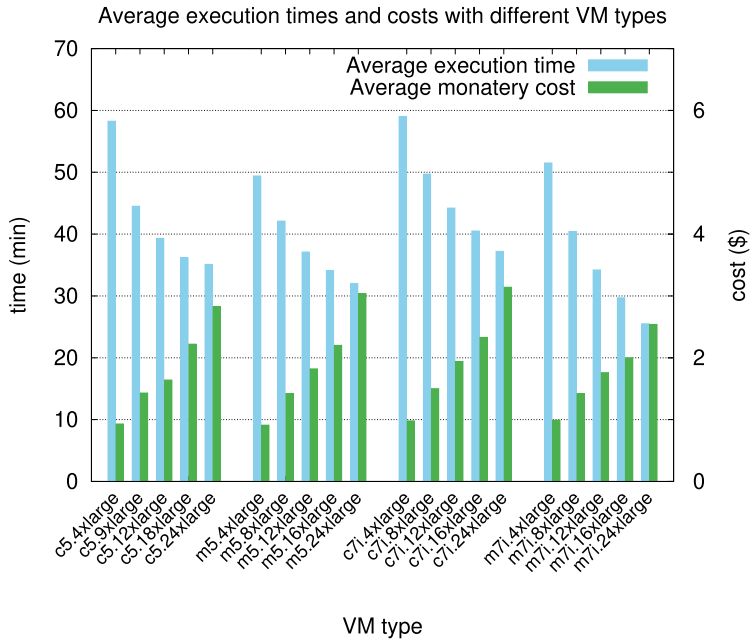

Fig. 16 Graphical comparison of the average execution times and costs for different VM types on AWS-EC2

mental study on the AWS-EC2 cloud platform. Table 9 shows the average times required to run the workflow on various VM types and the monetary costs for using the VMs, based on the pay-per-use provisioning model of AWS-EC2. Figure 16 shows a graphical comparison of data reported in Table 9. Data refers to four different VM families and to 20 different VM types, totally. Overall, they offer insights about times and operating costs of the procedure on AWS-EC2.

Acknowledgements The work presented in this article is partially funded by the following research projects: POR FESR Lazio 2014-2020 "Progetti di Gruppi di Ricerca 2020" Project ID (CUP) E85F21000940002.

Author Contributions C.V. contributed to conceptualization, investigation, workflow design and writing of the article, F. V. contributed to software development, L.G. contributed to conceptualization and supervision, P. D. coordinated the research work and contributed to supervision, software design and writing of the article. All authors contributed to the experimental evaluation and revised the manuscript.

Funding Open access funding provided by Università degli Studi Roma Tre within the CRUI-CARE Agreement. The work presented in this article was partially funded by Regione Lazio under the funding programme POR FESR Lazio 2014-2020 "Progetti di Gruppi di Ricerca 2020", Project ID (CUP) E85F21000940002.

Data Availability No datasets were generated or analysed during the current study.

Declarations

Competing interests The authors declare no competing interests.

References

Amazon (2024) Amazon Web Services. https://aws.amazon.com/. [Online; Accessed 5-Sept-2024]

Anand A, Imasu R, Dhaka SK et al (2024) Domain adaptation of deep learning segmentation model of small agricultural burn area detection using hi-resolution sentinel-2 observations: A case study of Punjab, India. In: EGU General Assembly, EGU

Apache (2024) Airflow 2.7.0. https://airflow.apache.org/. [Online; Accessed 5-Sept-2024]

Arjasakusuma S, Kusuma SS, Vetrita Y et al (2022) Monthly burned-area mapping using multi-sensor integration of sentinel-1 and sentinel-2 and machine learning: case study of 2019's fire events in south sumatra province, Indonesia. Remote Sens Appl Soc Environ 27:100790. https://doi.org/10.1016/j.rsase.2022.100790

Arnaudo E, Barco L, Merlo M et al (2023) Robust burned area delineation through multitask learning. In: Joint european conference on machine learning and knowledge discovery in databases. Springer, pp 436–447

Belenguer-Plomer MA, Tanase MA, Fernandez-Carrillo A et al (2019) Burned area detection and mapping using sentinel-1 backscatter coefficient and thermal anomalies. Remote Sens Environ 233:111345. https://doi.org/10.1016/j.rse.2019.111345. https://www.sciencedirect.com/science/article/pii/S0034425719303645

Brown AR, Petropoulos GP, Ferentinos KP (2018) Appraisal of the sentinel-1 & 2 use in a large-scale wildfire assessment: A

case study from portugal's fires of 2017. Appl Geogr 100:78–89. https://doi.org/10.1016/j.apgeog.2018.10.004. https://www.sciencedirect.com/science/article/pii/S0143622818305393

Chen Y, Morton DC, Randerson JT (2024) Remote sensing for wildfire monitoring: insights into burned area, emissions, and fire dynamics. One Earth 7(6):1022–1028

Cohen J (1960) A coefficient of agreement for nominal scales. Educ Psychol Meas 20(1):37–46

DIAS (2024) Copernicus data and information access services. https://www.copernicus.eu/en/access-data/dias. [Online; Accessed 5-Sept-2024]

Dindaroglu T, Babur E, Yakupoglu T et al (2021) Evaluation of geomorphometric characteristics and soil properties after a wildfire using sentinel-2 msi imagery for future fire-safe forest. Fire Saf J 122. https://doi.org/10.1016/J.FIRESAF.2021.103318

Docker (2024) Docker container. https://www.docker.com/resources/what-container/. [Online; Accessed 5-Sept-2024]

Donezar U, De Blas T, Larrañaga A et al (2019) Applicability of the multitemporal coherence approach to sentinel-1 for the detection and delineation of burnt areas in the context of the copernicus emergency management service. Remote Sens 11(22). https://doi.org/10.3390/rs11222607. https://www.mdpi.com/2072-4292/11/22/2607

ESA (2024a) esa-snappy. https://step.esa.int/main/download/snap-download/. [Online; Accessed 5-Sept-2024]

ESA (2024b) esa-snappy. https://github.com/senbox-org/esa-snappy. [Online; Accessed 17-Sept-2024]

EU (2024) Copernicus. https://www.copernicus.eu/. [Online; Accessed 5-Sept-2024]

Fernández-Manso A, Fernãndez-Manso O, Quintano C (2016) Sentinel-2a red-edge spectral indices suitability for discriminating burn severity. Int J Appl Earth Obs Geoinf 50:170–175. https://doi.org/10.1016/j.jag.2016.03.005.https://www.sciencedirect.com/science/article/pii/S0303243416300368

Gibson RK, Mitchell A, Chang HC (2023) Image texture analysis enhances classification of fire extent and severity using sentinel 1 and 2 satellite imagery. Remote Sens 15(14). https://doi.org/10.3390/rs15143512. https://www.mdpi.com/2072-4292/15/14/3512

Giglio L, Descloitres J, Justice CO et al (2003) An enhanced contextual fire detection algorithm for modis. Remote Sens Environ 87(2):273–282. https://doi.org/10.1016/S0034-4257(03)00184-6. https://www.sciencedirect.com/science/article/pii/S0034425703001846

Giorgos Mallinis IM, Chrysafi I (2018) Evaluating and comparing sentinel 2a and landsat-8 operational land imager (oli) spectral indices for estimating fire severity in a mediterranean pine ecosystem of greece. GISci Remote Sens 55(1):1–18. https://doi.org/10.1080/15481603.2017.1354803

Google (2024) Google cloud. https://cloud.google.com/. [Online; Accessed 5-Sept-2024]

Huang H, Roy DP, Boschetti L et al (2016) Separability analysis of sentinel-2a multi-spectral instrument (msi) data for burned area discrimination. Remote Sens 8(10). https://doi.org/10.3390/rs8100873. https://www.mdpi.com/2072-4292/8/10/873

Imperatore P, Azar R, Calò F et al (2017) Effect of the vegetation fire on backscattering: An investigation based on sentinel-1 observations. IEEE J Sel Top Appl Earth Obs Remote Sens 10(10):4478–4492. https://doi.org/10.1109/JSTARS.2017.2717039

Kim B, Lee K, Park S (2024) Burned-area mapping using post-fire planetscope images and a convolutional neural network. Remote Sens 16(14):2629

Knopp L, Wieland M, Rättich M et al (2020) A deep learning approach for burned area segmentation with sentinel-2 data. Remote Sens 12(15).https://doi.org/10.3390/rs12152422. https://www.mdpi.com/2072-4292/12/15/2422

Kurbanov E, Vorobev O, Lezhnin S et al (2022) Remote sensing of forest burnt area, burn severity, and post-fire recovery: a review. Remote Sens 14(19). https://doi.org/10.3390/rs14194714. https://www.mdpi.com/2072-4292/14/19/4714

Laneve G, Di Fonzo M, Pampanoni V et al (2023) Progress and limitations in the satellite-based estimate of burnt areas. Remote Sens 16(1):42

Lasaponara R, Tucci B (2019) Identification of burned areas and severity using sar sentinel-1. IEEE Geosci Remote Sens Lett 16(6):917–921. https://doi.org/10.1109/LGRS.2018.2888641

Lima TA, Beuchle R, Langner A et al (2019) Comparing sentinel-2 msi and landsat 8 oli imagery for monitoring selective logging in the brazilian amazon. Remote Sens 11(8). https://doi.org/10.3390/rs11080961. https://www.mdpi.com/2072-4292/11/8/961

Liu P, Liu Y, Guo X et al (2023) Burned area detection and mapping using time series sentinel-2 multispectral images. Remote Sens Environ 296:113753

Lopes A, Touzi R, Nezry E (1990) Adaptive speckle filters and scene heterogeneity. IEEE Trans Geosci Remote Sens 28(6):992–1000. https://doi.org/10.1109/36.62623

Navarro G, Caballero I, Silva G et al (2017) Evaluation of forest fire on madeira island using sentinel-2a msi imagery. Int J Appl Earth Obs Geoinf 58:97–106. https://doi.org/10.1016/j.jag.2017.02.003. https://www.sciencedirect.com/science/article/pii/S0303243417300296

Phiri D, Simwanda M, Salekin S et al (2020) Sentinel-2 data for land cover/use mapping: a review. Remote Sens 12(14). https://doi.org/10.3390/rs12142291. https://www.mdpi.com/2072-4292/12/14/2291

Rokhmatuloh, Ardiansyah, Indratmoko S et al (2022) Burnt-area quick mapping method with synthetic aperture radar data. Appl Sci 12(23). https://doi.org/10.3390/app122311922. https://www.mdpi.com/2076-3417/12/23/11922

Roy D, Jin Y, Lewis P et al (2005) Prototyping a global algorithm for systematic fire-affected area mapping using modis time series data. Remote Sens Environ 97(2):137–162. https://doi.org/10.1016/j.rse.2005.04.007. https://www.sciencedirect.com/science/article/pii/S0034425705001136

Roy DP, Boschetti L, Justice CO (2007) The global modis burned area product. Towards an Operational use of Remote Sensing in Forest Fire Management p 191

Santi E, Paloscia S, Pettinato S et al (2017) The potential of multifrequency sar images for estimating forest biomass in Mediterranean areas. Remote Sens Environ 200:63–73. https://doi.org/10.1016/j.rse.2017.07.038. https://www.sciencedirect.com/science/article/pii/S003442571730353X

Seo Y, Lee Y (2024) A comparative analysis of cnn and transformer models for the detection of fire-burned areas in California using landsat 8 satellite images. In: IGARSS 2024-2024 IEEE International geoscience and remote sensing symposium. IEEE, pp 7071–7075

Smiraglia D, Filipponi F, Mandrone S et al (2020) Agreement index for burned area mapping: Integration of multiple spectral indices using sentinel-2 satellite images. Remote Sens 12(11). https://doi.org/10.3390/rs12111862. https://www.mdpi.com/2072-4292/12/11/1862

Tanase MA, Santoro M, Wegmüller U et al (2010) Properties of x-, c- and l-band repeat-pass interferometric sar coherence in Mediterranean pine forests affected by fires. Remote Sens Environ 114(10):2182–2194. https://doi.org/10.1016/j.rse.2010.04.021. https://www.sciencedirect.com/science/article/pii/S0034425710001343

Tanase MA, Belenguer-Plomer MA, Roteta E et al (2020) Burned area detection and mapping: Intercomparison of sentinel-1 and sentinel-2 based algorithms over tropical Africa. Remote

Sens 12(2). https://doi.org/10.3390/rs12020334. https://www.mdpi.com/2072-4292/12/2/334

Tariq A, Shu H, Li Q et al (2021) Quantitative analysis of forest fires in southeastern Australia using sar data. Remote Sens 13(12). https://doi.org/10.3390/rs13122386. https://www.mdpi.com/2072-4292/13/12/2386

Zhang Q, Ge L, Zhang R et al (2021) Deep-learning-based burned area mapping using the synergy of sentinel-1&2 data. Remote Sens Environ 264:112575. https://doi.org/10.1016/j.rse.2021.112575. https://www.sciencedirect.com/science/article/pii/S0034425721002959